



# Synthesis, characterization, and temperature-dependent electronic properties of ZnO nanorods using CBD techniques

C. A. Ruiz-Rojas<sup>1</sup>, M. Aguilar-Frutis<sup>1\*</sup> , F. Ramos-Brito<sup>2</sup>, I. A. Garduño-Wilches<sup>3</sup>, J. Narro-Ríos<sup>4</sup>, L. Lartundo-Rojas<sup>5</sup>, and G. Alarcón-Flores<sup>1</sup>

<sup>1</sup>Centro de Investigación en Ciencia Aplicada y Tecnología Avanzada, Instituto Politécnico Nacional, Calzada Legaria 694, Col. Irrigación, Alcaldía Miguel Hidalgo, 11500 Ciudad de México, Mexico

<sup>2</sup>Laboratorio de Síntesis de Materiales-Facultad de Ciencias Físico-Matemáticas-Universidad Autónoma de Sinaloa, Ciudad Universitaria s/n, 80000 Culiacán Sinaloa, Mexico

<sup>3</sup>Centro de Investigación en Ciencia Aplicada y Tecnología Avanzada, Cátedras Conacyt/Instituto Politécnico Nacional, Calzada Legaria 694, Col. Irrigación, Alcaldía Miguel Hidalgo, 11500 Ciudad de México, Mexico

<sup>4</sup>Centro de Investigación en Ciencia Aplicada Y Tecnología Avanzada, Estancia Postdoctoral/Instituto Politécnico Nacional, Calzada Legaria 694, Col. Irrigación, Del. Miguel Hidalgo, 11500 Ciudad de México, Mexico

<sup>5</sup>Centro de Nanociencias y Micro y Nanotecnologías, Unidad Profesional Adolfo López Mateos, Instituto Politécnico Nacional, Luis Enrique Erro s/n, Col. Zacatenco, 07738 Ciudad de México, Mexico

Received: 31 October 2020

Accepted: 16 February 2021

Published online:

7 March 2021

© The Author(s), under exclusive licence to Springer Science+Business Media, LLC, part of Springer Nature 2021

## ABSTRACT

High-quality and partially oriented ZnO nanorod films were synthesized by chemical bath deposition on top of a ZnO sol-gel spin-coating seed layer deposited on glass substrates. Two different ratios (0.625 and 6.25) of hexamethylenetetramine to zinc acetate were considered for the synthesis of the ZnO nanorod films and their optical, structural and electronic properties were studied. The ZnO nanorod films showed the wurtzite structure with a crystallite size about 50–55 nm, a dislocation density in the range of  $10^{15}$  lines-m<sup>-2</sup> and a strain in the range of  $10^{-3}$ . Energy dispersive spectroscopy and photoluminescence measurements indicated the existence of oxygen vacancies in the films. The ZnO nanorod films showed a bandgap energy about 3.24 eV. From photoluminescence results, an intense ultraviolet excitonic emission band was observed in the films. The films resulted with a carrier concentration in the range of  $10^{15}$  and  $10^{16}$  cm<sup>-3</sup>. From impedance spectroscopy measurements, a noticeable temperature-dependent electronic conductivity was observed, related probably to the nanostructured morphology of the films. In both films it was observed that the electronic conductivity decreased in the intermediate temperature region with the increment of temperature, probably due to chemisorption or desorption phenomena. But the electronic conductivity in the low and the high-temperature regions obeyed the grain boundary carrier-

Address correspondence to E-mail: maguilarf@ipn.mx

trapping model with the increment of the temperature, showing in both regions an activation energy close to 0.6 eV, attributed to the appearance of trap states due to the chemisorption of oxygen at the grain boundaries of the ZnO nanorods.

## 1 Introduction

Zinc oxide (ZnO) is an important wide bandgap compound semiconductor ( $E_g = 3.37$  eV) which has been investigated for decades. ZnO belongs to the group of transparent conductor oxides (TCO's) showing also a lot of applications in industry. Fundamental and applied research in ZnO emerged due to the prospective use of ZnO as an optoelectronic material for blue and UV lasers [1, 2]. ZnO in thin film is of paramount importance in most thin film solar cells [3, 4]. In fact, cost-effective large-scale production of ZnO thin films and the development of them with improved properties are key challenges in the field of production and R & D in photovoltaics. Actually, scientific challenges include the development of nanostructured ZnO films, like ZnO nanorods and p-type ZnO films which may both open new possibilities for designing future thin film solar cells [3]. Since the last couple of decades, several techniques have been used to grow ZnO nanostructured films; techniques such as pulsed laser ablation [5–7], magnetron sputtering [8–10], RF sputtering [11], chemical vapor deposition [12–14], and chemical solution preparation [15, 16]. Within the latter technique, it is highlighted the work of Abdulrahman et al. who synthesized ZnO nanorods using conventional and modified chemical bath deposition methods, showing improved characteristics of the ZnO nanorods [17]. Different morphologies for ZnO have been obtained; ZnO nanorods [15, 18–20], ZnO nanodots [21, 22], ZnO nanobelts [23–25], ZnO nanotubes [3, 12], or ZnO in cauliflower shape [3, 26]. Microrods or nanorods of ZnO have been highlighted because of their physical properties like quantum confinement [20]. These nanostructures result suitable to study several of their properties, for example, their electrical transport mechanisms, which results important for the development of new devices with high performance and efficiency. In photovoltaic devices [3], ZnO-oriented nanorods have shown an important cell efficiency [4, 19]. In addition, light emission diodes fabricated with ZnO-oriented nanorods show

very noticeable characteristics [27–29]. For the latter reasons, we focused in this work on the synthesis by simple routes, and on the characterization of ZnO nanorod films. Both, the spin-coating method and the chemical bath deposition (CBD) techniques were used to obtain the ZnO buffer layer and the ZnO nanorod film, respectively. The ZnO buffer layer acted as an essential (seed) layer to promote the precipitation of the nanorods of ZnO on top [2]. Upon the growth of the ZnO nanorods, their electronic transport characteristics, as well as their optical and structural properties were conducted. It is emphasized the temperature-dependent electrical conductivity of the ZnO nanorod precipitates, as well as other optical and structural features. The CBD technique was chosen for the ZnO nanorod synthesis because it leads to stable, adherent, uniform and hard nanomaterials and thin films with good reproducibility and at relatively low temperature [30, 31]. It is highlighted in this work the temperature-dependent electrical conductivity of the ZnO nanorod films, studied by impedance spectroscopy, showing three regions of conductivity, probably related to surface effects of the nanostructured films. In addition, the films resulted clean and with certain orientation along the c-axis direction. The optical bandgap, computed from photoluminescence measurements, was about 3.2 eV. The recombination band associated to excitons was clearly present in the different samples. Finally, Hall effect van der Pauw characterization was also carried out.

## 2 Experimental details

The ZnO buffer layer (or seed layer) was obtained by the spin-coating technique from a 0.06 M solution of zinc acetate dehydrate “ZnAc”  $\text{Zn}(\text{CH}_3\text{COO})_2 \cdot 2\text{H}_2\text{O}$  (Sigma Aldrich Co.) and methanol (J.T. Baker) on glass substrates. The glass substrates were ultrasonically cleaned in several solvents: methanol, acetone and isopropanol (J.T. Baker). Finally, they were rinsed in deionized water and dried with a nitrogen

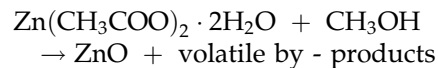
flow prior to deposition of the ZnO buffer layer. The solution was heated at 50 °C and stirred for 10 min. Then the solution was dropped on the glass substrate making use of a micro-pipette and then was spun at 2800 RPM for 30 s to get the ZnO buffer layers. The deposited ZnO buffer layers were then annealed in a furnace using a heating ramp rate of 5 °C·min<sup>-1</sup>, considering the following sequence: an initial annealing was done at 150 °C for 40 min, then, an annealing at 300 °C during other 40 min, and finally, a last annealing at 450 °C for 90 min. Upon the deposition of the ZnO buffer thin film, the thick ZnO nanorods film was grown on top by Chemical Bath Deposition (CBD) from a 0.024 M solution of ZnAc and Hexamethylenetetramine “HMTA” ((CH<sub>2</sub>)<sub>6</sub>N<sub>4</sub>) (J. T. Baker). Two concentrations of HMTA were considered: 0.015 M and 0.15 M. For this task, to prepare the chemical bath solution, deionized water, the source of zinc and the HMTA were poured inside a baker. To get a good mixture, the baker was placed on top a magnetic agitation device for 10 min, and it was placed later inside an ultrasonic cleaning system for 5 min. In this way, two different ratios and very apart of HMTA to ZnAc (HMTA:ZnAc) were considered to get the films: An 0.625:1 ratio was used to prepare F1 films and an 6.25:1 ratio to prepare F2 films. The chemical bath solution of HMTA:ZnAc was set at ~ 77 °C, and the elapsing time to get the ZnO films was fixed in 12 h. The surface morphology of the films was studied by Scanning Electron Microscopy (SEM, JEOL JSM-6390LV) and Atomic Force Microscopy (AFM, JEOL JSMP-4210). The elemental chemical composition of the films was studied by Energy Dispersive Spectroscopy (Inca X-sight from Oxford Instruments). The thickness of the films was obtained by Profilometry (Veeco, Dektak<sup>3</sup>). The structural properties were analyzed by X-ray diffraction (Bruker D8 Advance, Diffractometer), using the Cu k<sub>α1</sub> (λ = 1.542 Å) at a grazing angle of 0.5° and step-rate of 0.6° min<sup>-1</sup>. Diffuse reflectance and Photoluminescence properties were obtained in a spectrofluorometer (Edinburgh Instruments, FS5 model). The resistivity, mobility and carrier density were obtained in a ECOPIA HMS-3000 Hall Effect System. Impedance spectroscopy measurements were carried out in a Solartron 1260A Frequency Response Analyzer as a function of temperature and at ambient pressure. The frequency range used was between 1 MHz and 1 Hz. A 20 mV ac signal was considered and a dc voltage of 0 V was fixed. The

films were measured in coplanar configuration using silver paint as electrodes. All the readings were acquired after the sample in turn reached the thermal equilibrium at the selected set point. We waited about 15–20 min between each reading. The different readings were registered at each temperature in steps of ~ 15 K. The measurements were carried out from room temperature up to ~ 673 K.

### 3 Results and discussion

#### 3.1 Structural properties

Figure 1 shows the typical AFM surface morphology of a ZnO buffer layer obtained by spin-coating using zinc acetate dehydrate, as a first step. Literature has reported the preference of using the latter reagent to obtain zinc oxide because acetate groups, as contaminants, decompose under annealing producing combustion volatile by-products from zinc acetate dehydrate [32]. The chemical reaction proposed for can be simply depicted as follows:



This type of seeding produced probably ZnO nanocrystals that looked grainy distributed uniformly on top of the substrate that appeared in the range of some tenths of nanometers, Fig. 1. This result is in agreement with the work of Song et al. [33] and of Son et al. [34], who found that the ZnO nanorods are strongly influenced by the seed layer; its crystal size and surface roughness, showing that the average diameter of the nanorods is found in the

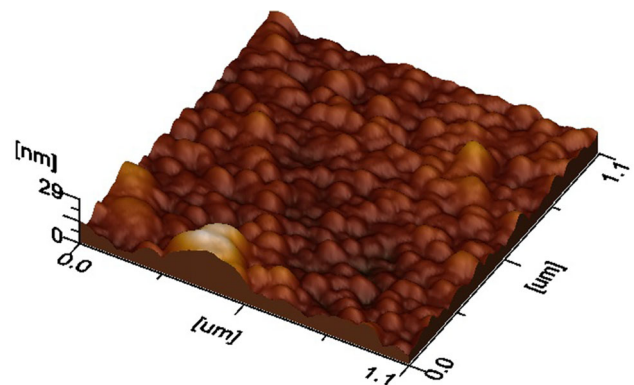


**Fig. 1** Typical atomic force microscopy image of the surface morphology of a ZnO buffer layer deposited by spin-coating on top of the glass substrate

range of the average grain size of ZnO thin films and roughness. In Fig. 1, the grainy nature of the seed layer in our work probably facilitated the engineering of the vertically aligned ZnO nanorod arrays, confirming the important role of ZnO film as a seed layer for the vertical growth of ZnO nanorods. This step has resulted essential to promote the one-dimensional (*c*-axis oriented) growth of crystalline ZnO nanostructures [15, 33, 35, 36]. Cui et al. [37], considered a similar type of seeding to get ZnO nanowire arrays. Literature shows that the seeding has been successful considering different techniques such as: Sol–gel [38], sputtering [39], sol–gel spin-coating [40], electrochemical deposition [41], etc. However, other works have considered as seed layer a thin film of Ag<sup>0</sup> deposited by electron beam on silicon substrates to promote the *c*-axis oriented nanorods [42]. In our case, the spin-coating technique seems to result favorably as well. As a second step, the ZnO nanorod layer was grown by CBD on top of the seed ZnO layer. Figure 2a and b, as well as Fig. 3a and b, show the SEM images in cross section and planar views, respectively, for ZnO nanorod thin films F1 and F2 grown by CBD on top of the seed ZnO layer. The films grown showed the nanorod shape structure with a certain degree of orientation. Making use of the Image-J program we estimated the height and length of the ZnO precipitates in both films. The histograms of size distribution are shown next to Figs. 2a, b, 3a and b. In resume, the length and diameter for nanorods in film F1 are  $1152 \pm 135$  nm and  $156 \pm 30$  nm, respectively, and  $1642 \pm 230$  nm and  $345 \pm 46$  nm in film F2, respectively. The nanorods for film F1 were thinner and shorter, probably because of this reason they looked randomly oriented, appearing like ZnO nanorod precipitation. The growth rate of the ZnO nanorods is estimated about  $96 \text{ nm}\cdot\text{h}^{-1}$  and  $137 \text{ nm}\cdot\text{h}^{-1}$ , for films F1 and F2, respectively. The larger the size distribution and growth rate of nanorods in film F2 was probably due to the higher concentration of HMTA used to synthesize this film. It is also noticed that a better looking aspect of ZnO nanorods in film F2 was obtained. From Figs. 2a and 3b, an approximate surface-to-volume ratio ( $A/V$ ) of the ZnO nanorods could be computed considering the average length and diameter of the rods and using the equation  $\frac{A}{V} \sim \frac{(D+4L)}{LD}$ , where  $D$  is the diameter and  $L$  is the length of the rods. For F1 films this ratio is about

$26.5 \times 10^4 \text{ cm}^{-1}$  and for F2 film about  $12.2 \times 10^4 \text{ cm}^{-1}$ . ZnO nanorods for film F1 show approximately a twice surface-to-volume ratio compared to ZnO nanorods for film F2. This result might probably lead to slight differences in their properties. The formation of oriented ZnO films has been addressed in the literature [32, 43]. The conclusion is that orientation is essentially a matter of nucleation and crystal growth that is explained by the influence of the substrates regardless of epitaxial or non-epitaxial growth [38, 43]. Ashfold et al. [44] studied the kinetics of the hydrothermal growth of ZnO nanostructures involving the reaction between HMTA and aqueous zinc ions. According to his work, an important path in the reaction for the formation of zinc oxide nanoparticle arrays are the thermal decomposition of HMTA and the precipitation of Zn<sup>2+</sup> ions. They stated that HMTA acted as a source of hydroxide (OH<sup>1-</sup>) increasing the solution pH to drive the precipitation reaction of Zn(OH)<sub>2</sub>; however, they stated the possibility that the role of HMTA was that of a buffer too. In our case, we considered the reaction between zinc acetate dehydrate and HMTA to get the partially ZnO-oriented nanorods, using the chemical bath deposition technique. A further work considering the kinetics of the chemical growth of ZnO nanorods needs to be addressed. Nevertheless, according to the synthesis conditions, it is possible to appreciate that the nanorods present noticeable geometrical dimensions where the area-to-volume ratio is large. This feature seems to be of great importance because of its associated surface effects that might have a strong influence on the overall electrical and optical properties [45]. From Fig. 2b, the nanorods appeared to be thinner in diameter when synthesized with the lowest amount of HMTA in solution (film F1). It is noticeable that the characteristic hexagonal structure of ZnO is better appreciated in the sample synthesized with the highest concentration of HMTA (film F2), Fig. 3b. The elemental composition of the films was analyzed by Energy Dispersive Spectroscopy. The at% Zn was always higher than the at% O in the films, consequently, its ratio is higher than one, but it approached to this value as the concentration of HMTA increased. Table 1 resumes the elemental composition of the films, as well as additional properties of the films studied in this work. A better stoichiometry is obtained in the films deposited with a larger amount of HMTA in solution. Since the at% of Zn is higher than 50, it is possible that the

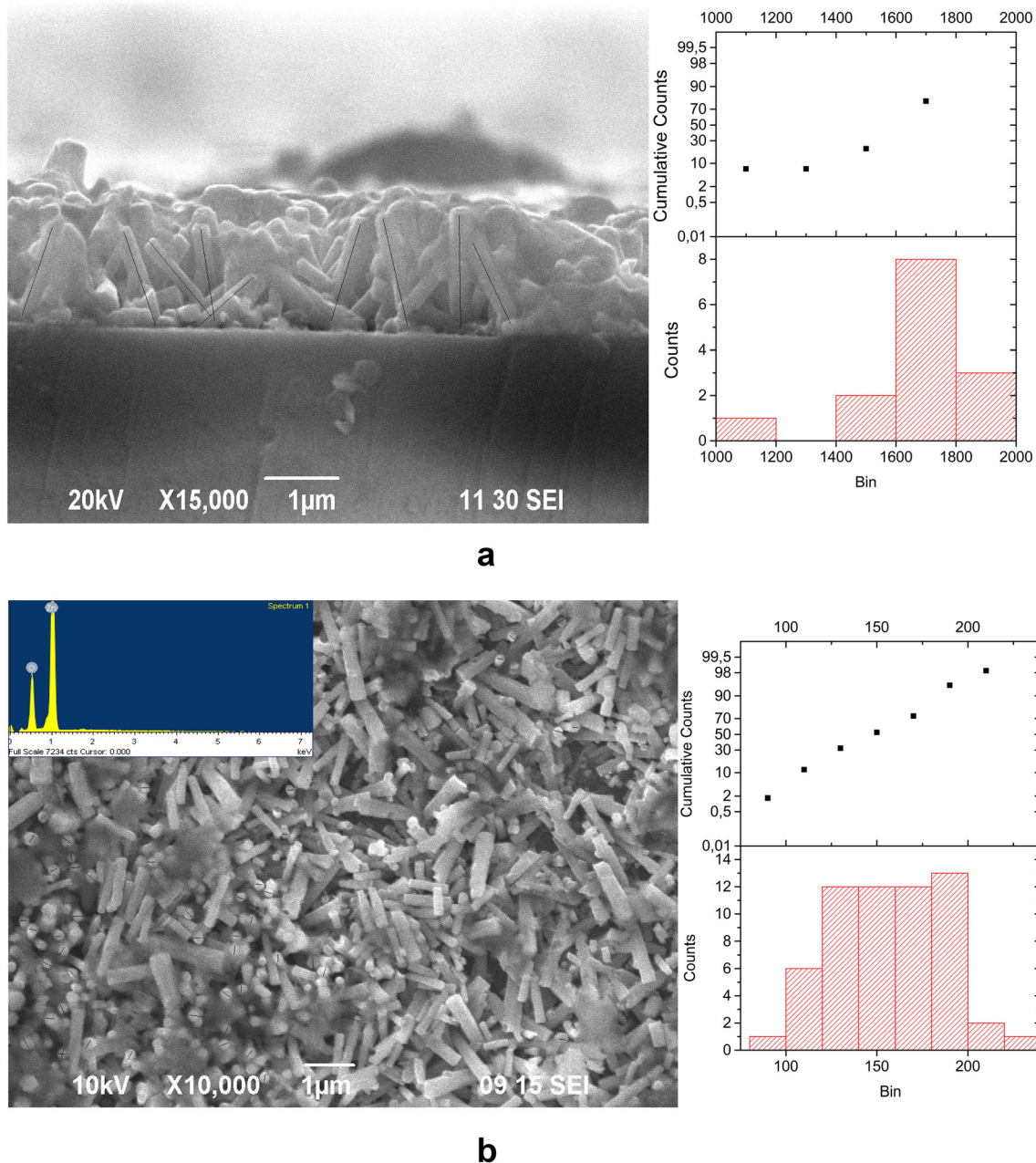


**Fig. 2** **a** Scanning electron microscopy image of the surface morphology of a ZnO nanorod thin film (Film F1) observed in cross section view. The histogram on the right represents the size distribution of the nanorods. **b** Scanning electron microscopy

image of the surface morphology of a ZnO nanorod thin film (Film F1) observed in planar view. The histogram on the right represents the size distribution of the nanorods. The inset shows the EDS spectrum

excess in zinc is probably related to interstitial zinc, at the same time, the amount of oxygen was lower than 50 at%, this deficiency might be related to oxygen vacancies. The latter natural defects in ZnO have been extensively discussed in the literature, and it is worth to mention that the deposition method of ZnO is very dramatic in its dependence to the type and

amount of natural defects. Many structural defects have been predicted in this type of oxide; in addition to the above mentioned; zinc vacancies  $V_{zn}$ , interstitial oxygen  $O_i$ , as well as antisite defects have been reported [46], making the defect structure in ZnO very complex. In resume, the ZnO nanorods synthesized in this work inherently resulted with interstitial

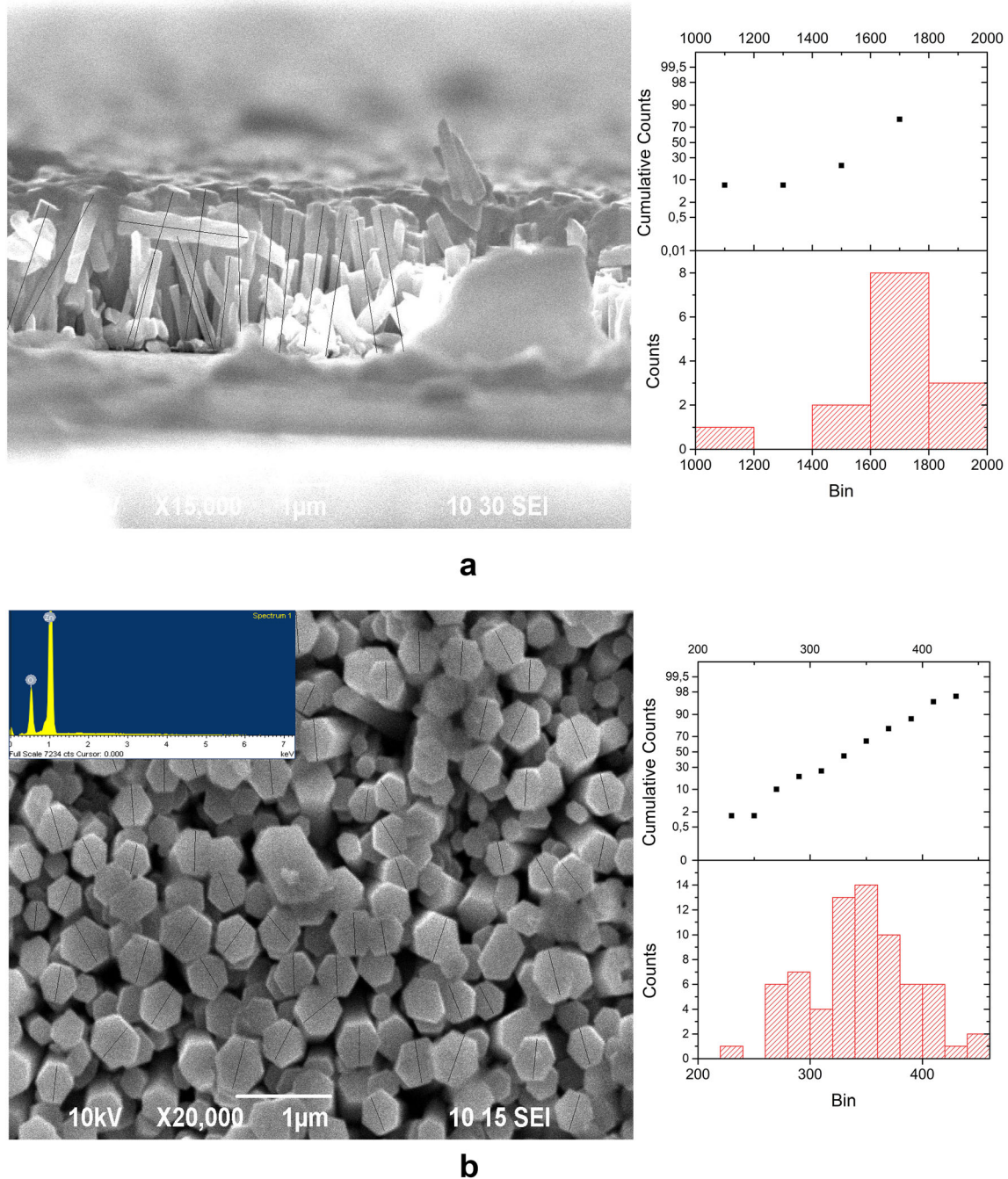


**Fig. 3** **a** Scanning electron microscopy image of the surface morphology of a ZnO nanorod thin film (Film F2) observed in cross section view. The histogram on the right represents the size distribution of the nanorods. **b** Scanning electron microscopy

image of the surface morphology of a ZnO nanorod thin film (Film F2) observed in planar view. The histogram on the right represents the size distribution of the nanorods. The inset shows the EDS spectrum

zinc and/or oxygen vacancies as natural defects, but free from any other contaminants or by-products of the reaction, as suggested by Znaidi [32], when using zinc acetate hydrate as source of zinc. Figure 4 shows the X-ray diffraction patterns of the as deposited of

ZnO nanorod films. The X-ray reflections that can be appreciated matched appropriately to the ZnO diffraction card in its wurtzite phase (JCPDS-00-036-1451). A polycrystalline character can be seen in the films, but orientation along the (002) plane (c-axis

**Table 1** Main structural, optical and electronic characteristics of ZnO nanorod thin films

ZnO nanorod film	HMTA:ZnAc ratio	Elemental composition	Structural characteristics				Photoluminescence characteristics	Electronic characteristics
			L (nm)	Lattice parameters	$\delta/$ ( $10^{14}$ lines- $m^{-2}$ )	$\varepsilon/$ ( $10^{-4}$ )		
F1	0.625	at % Zn = 55.8 at % O = 44.2 $\frac{[Zn]}{[O]}$ ratio = 1.3	~ 50	$a = 3.2502 \text{ \AA}$ , $c = 5.2051 \text{ \AA}$  $d_{(200)} = 2.606 \text{ \AA}$	14.2	12.9	~ 319 nm (exciton) ~ 436, 515 nm ( $V_O$ defects) ~ 620 nm (defect band) ~ 1.2 (ratio between exciton and defect band maximum intensities)	Hall Effect $n = 3 \times 10^{15} \text{ cm}^{-3}$ $\mu = 39 \frac{\text{cm}^2}{\text{Vs}}$ $\rho = 659 \Omega - \text{cm}$  Impedance spectroscopy $0.65 \pm 0.01 \text{ eV}$ (low-temperature region) $0.67 \pm 0.02 \text{ eV}$ (high-temperature region)
F2	6.25	at % Zn = 51.7 at % O = 48.3 $\frac{[Zn]}{[O]}$ ratio = 1.1	~ 55	$a = 3.2508 \text{ \AA}$ , $b = 5.2001 \text{ \AA}$  $d_{(200)} = 2.610 \text{ \AA}$	13.1	12.4	~ 319 nm (exciton) ~ 436 nm ( $V_O$ defects) ~ 620 nm (wide defect band) ~ 0.6 (ratio between exciton and defect band maximum intensities)	Hall Effect $n = 7.5 \times 10^{16} \text{ cm}^{-3}$ $\mu = 29 \frac{\text{cm}^2}{\text{Vs}}$ $\rho = 307 \Omega - \text{cm}$  Impedance spectroscopy $0.77 \pm 0.04 \text{ eV}$ (low-temperature region) $0.65 \pm 0.06 \text{ eV}$ (high-temperature region)

orientation,  $2\Theta = 34.3^\circ$ ), was the most intense in both diffraction patterns. This result is in agreement with the result from Abdulrahman [47] who suggested that ZnO nanorods synthesized by CBD method tend to grow along the (002) preferred orientation because of the lowest surface energy density associated with this direction. However, it is not discarded that the crystallinity of the ZnO nanorods might be strongly influenced also by the orientation of the seed layer, Son et al. [34]. The preferred orientation in the films is reinforced by the experimental observation related to the nanorod morphology of the films. Furthermore, the diffraction pattern for film F2 presents additional reflections located at  $2\Theta = 30.8^\circ$ ,  $31.6^\circ$ ,  $32.4^\circ$  and  $42.5^\circ$ . These reflections became more prominent as

the amount of HMTA increased in the solution. The reflection at  $2\Theta = 31.6^\circ$  is probably related to zinc hydroxide,  $\text{Zn}(\text{OH})_2$ , probably related to the role of the HMTA during the chemical reaction [44]. The crystallite size was estimated with the aid of the Scherrer equation:  $L = \frac{K\lambda}{\beta \cos \theta}$  where  $L$  is the average crystallite size,  $\lambda$  is the X-ray wavelength,  $\theta$  is the Bragg angle and  $\beta$  is the width at half maximum of the peak in radians. Considering the (002) reflection, an average value of 55 nm for film F2 and about 50 nm for film F1 was estimated for the crystallite size. These results are in agreement with previous works carried out [26, 48]. Furthermore, the lattice parameters  $a = b$  and  $c$  were estimated with the aid of the following equation for an hexagonal crystal

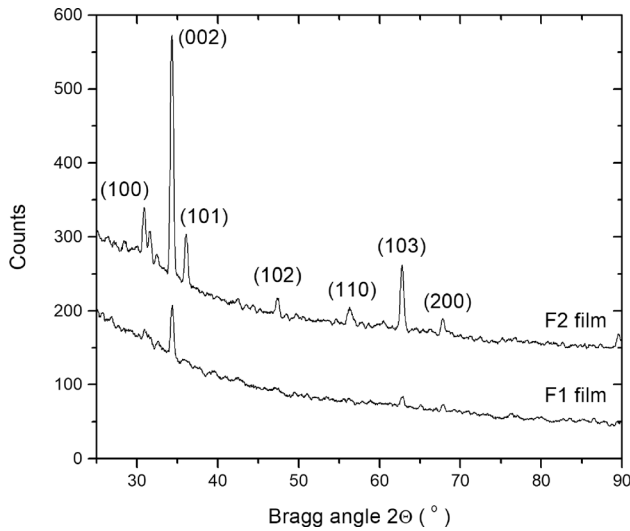


**Fig. 4** X-ray diffraction patterns of the ZnO nanorod thin films

system:  $\frac{1}{d^2} = \frac{4}{3} \left[ \frac{h^2 + hk + k^2}{a^2} \right] + \frac{l^2}{c^2}$ , where  $d$  is the interplanar distance. The dislocation density ( $\delta$ ), defined by the relation:  $\delta = \frac{1}{L^2}$ , was also estimated. The dislocation density is referred to the length of dislocation lines per unit volume. Finally, the strain ( $\epsilon$ ), was also estimated using the relation:  $\epsilon = \frac{\beta \cos \theta}{4}$  [49]. The lattice parameters for both films were similar, the dislocation density was in the range of  $10^{15}$  lines- $m^{-2}$  and the strain in the range of  $10^{-3}$ . These results are in agreement with the work of Raghu [49].

### 3.2 Optical properties

#### 3.2.1 Diffuse reflectance

Figure 5 shows the diffuse reflectance measurements of the ZnO nanorod films. From the figure it is observed that the absorption edge is located around 400 nm. The computation of the energy bandgap was estimated from the Kubelka–Munk function:  $F(R) = \frac{(1-R)^2}{2R}$ , where  $R$  is the absolute reflectance [50]. A plot of  $(F(R) * hv)^2$  as a function of the energy ( $hv$ ) yields a curve whose linear part is extrapolated to the energy axis and its intersection determined the energy bandgap. The bandgap energy was very similar in both samples, regardless of the amount of HMTA used in the solution for their synthesis, showing an average value of  $3.24 \pm 0.01$  eV. This bandgap value has been reported for ZnO in previous works [26, 48, 51].

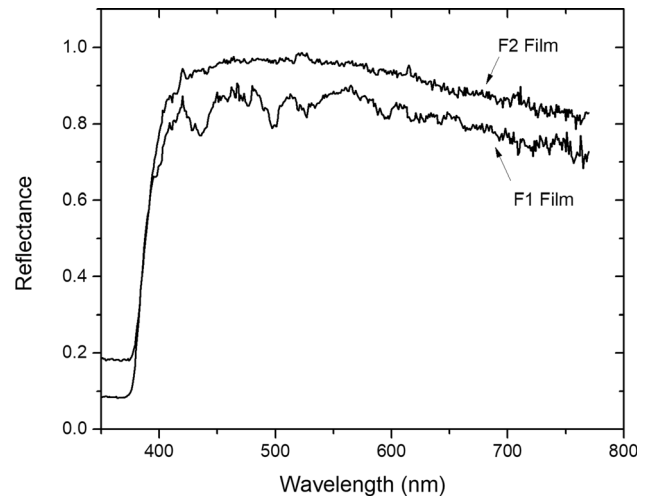


**Fig. 5** Optical reflectance as a function of the wavelength for the ZnO nanorod films

#### 3.2.2 Photoluminescence

Figure 6 shows the PL spectra for films F1 and F2. The different ZnO films were excited with  $\lambda_{\text{excitation}} = 325$  nm, to ensure the electron transition from the valence to the conduction band. From Fig. 6, it can be seen the emission of a narrow band ranging from 385 to 420 nm, approximately, reaching its maximum at about 391 nm (3.17 eV). Due to the sharpness of the band and because of its closeness to the bandgap energy (3.24 eV), such band can be attributed to an

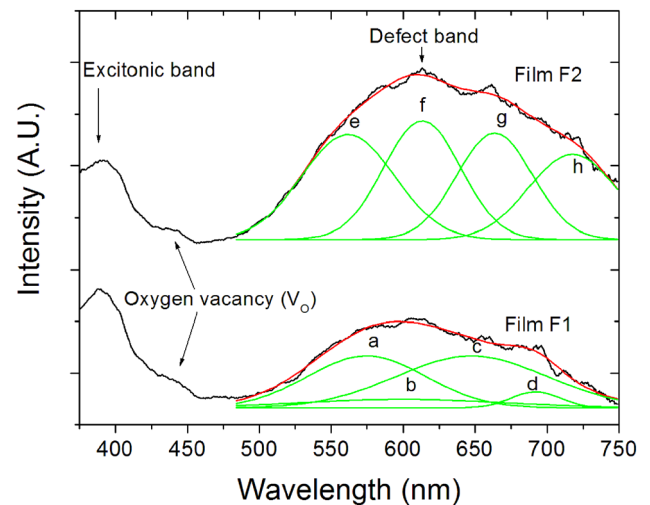


**Fig. 6** Photoluminescence spectra for the ZnO nanorod thin films. The defect band was de-convoluted considering four Gaussian peaks centered at: **a** 574.5 nm, **b** 599.5 nm, **c** 647.7 nm and **d** 692.1 nm, for nanorod film F1 and at **e** 561.8 nm, **f** 613.4 nm, **g** 663.7 nm and **h** 717.6 nm, for nanorod film F2



excitonic emission [52]. In addition to the latter band, it is observed another wide band located around 620 nm, the defect band. The PL emission of the latter band is clearly noticed to the naked eye and at room temperature. However, in film F1 the excitonic emission was more intense than the defect band, which was not the case for film F2. The ratio of the intensity between the excitonic band and the wide band was computed for each film and it was about 1.2 for film F1, and about 0.6 for film F2, indicating that the amount of HMTA probably influenced the optical properties of the films. The luminescent properties of ZnO thin films have been reported already in different works [26, 48, 51], nevertheless, the several conclusions that have been derived about this property are strongly dependent on the synthesis route of the films. For example, Mandal et al. [52] obtained high-quality ZnO nanorods by vapor–solid technique at 550°, 650° and 750 °C. In his work, besides the excitonic band, he observed the blue-green emission (located at 2.755–2.254 eV), due to the recombination of a photogenerated hole with the singly charged oxygen vacancy ( $V_O$ ). In our work, film F1 and probably film F2 too showed a band within this region, about 515 nm (2.408 eV), in agreement with the following computation:  $3.24 - 0.832 \text{ eV} = 2.408 \text{ eV}$ ; this indicates an emission due to traps from deep donor levels located at 0.832 eV, below the conduction band, to the edge of the valence band ( $E_V$ ). Mandal et al. reported that  $V_O$  is located below the conduction band at 0.8–1.0 eV. In addition, in our work, in both spectra, it can be appreciated a band located about 436 nm (2.842 eV). Carrying out a similar computation:  $3.24 \text{ eV} - 0.398 \text{ eV} = 2.842 \text{ eV}$ , it is suggested another transition that may originate from shallow donor levels, which according again to Mandal et al. are also due to  $V_O$  (0.4–0.6 eV below the conduction band), to the edge of the valence band. These results seem to support the existence of oxygen vacancies in our films. No other noticeable bands can hardly be appreciated, except for the wide emission band centered around 620 nm (ranging from 485 to 750 nm). However, its wideness makes difficult to resolve the different emission in that large spectral range. A de-convolution of the defect band was carried out considering Gaussian peaks. The best de-convolution process was obtained considering four peaks, shown in Fig. 5. The Origin program was used to carry out this task. In resume, the defect band in F1 film was de-convoluted in the bands located at

575 nm, 599 nm, 648 nm and 692 nm, approximately. And for the case of F2 film at 562 nm, 613 nm, 664 nm and 718 nm, approximately. Gogurla et al. [53] and Chakrabarty [54] resolved the defect band in ZnO. They proposed four peaks consisting of the green emission (510 nm), the yellow emission (580 nm), the orange-red emission (647 nm) and a tail in the infrared (734 nm), all related to several point defects in the ZnO. For example, the green emission has been associated with single ionized oxygen vacancies, the yellow emission is associated with a double ionized oxygen vacancy, the orange-red is associated with oxygen interstitials and the infrared tail has been attributed to the transition among two types of defects or complex defects. In our work the de-convoluted bands did not match exactly, or were shifted, compared to the ones already reported, except for the band located at 648 nm. However, it can be appreciated within the defect band, the one close to 510 nm, related to the oxygen vacancies. The PL spectrum for film F1 looked close to the high-quality ZnO nanorods obtained by Mandal et al. [52], and the spectrum for film F2 looked probably like bulk ZnO. Therefore, high-quality ZnO nanorods seem to be obtained with the lowest amount of HMTA during synthesis. Table 1 resumes the PL emission bands.

### 3.3 Electronic properties

The carrier concentration, Hall mobility and electrical resistivity of the different films as synthesized were obtained by Hall effect in the Van der Pauw configuration at room temperature. For this purpose, a 0.5  $\mu\text{A}$  dc current was applied during the measurements. The common n-type conductivity was verified in them. The carrier concentration in film F1 was about  $3 \times 10^{15} \text{ cm}^{-3}$  and  $7.5 \times 10^{16} \text{ cm}^{-3}$  in film F2, the mobility varied between 29  $\text{cm}^2/\text{Vs}$  for film F2 and 39  $\text{cm}^2/\text{Vs}$  for film F1 and the electrical resistivity was found between 300  $\Omega\text{-cm}$  for film F2 and 660  $\Omega\text{-cm}$  for film F1, as shown in Fig. 7. The higher resistivity in film F1 is in agreement with its lower carrier concentration. According to Swalin [55], the open character of the wurtzite structure in ZnO results in the existence of zinc ions in the interstitial sites as well as in the normal lattice sites. This results seems to be in agreement since it was found that in our case the ZnO films resulted non-stoichiometric,  $\frac{[\text{Zn}]}{[\text{O}]} > 1$ . Probably,

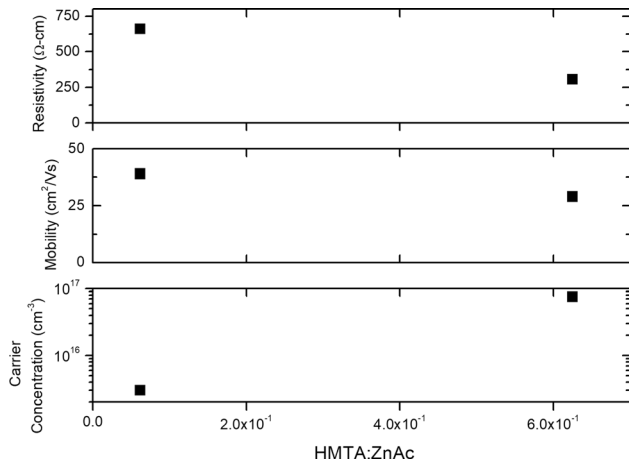


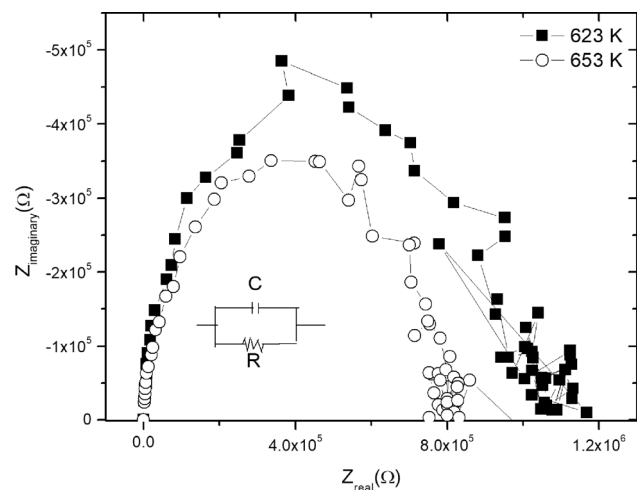
**Fig. 7** Hall results: resistivity, mobility and carrier concentration for the ZnO nanorod films measured

the concentration of electrons in the conduction band is associated to the excess of Zn. The formation of ionized cation interstitials is proposed to follow the reaction:  $Zn(g) = Zn_i + e$ . This donor level lies 0.05 eV below the conduction band and therefore the donors are completely ionized at room temperature as well as at higher temperatures [55]. The formation of anion vacancies with complete ionization of anion vacancy donors is not discarded in our work too, according to the following reaction:  $O_O = \frac{1}{2}O_2(g) + V_O + e$ , suggested by Swalin [55]. In our case, as a result of the non-stoichiometric, the electron concentration is probably due mainly to interstitial zinc and oxygen vacancies.

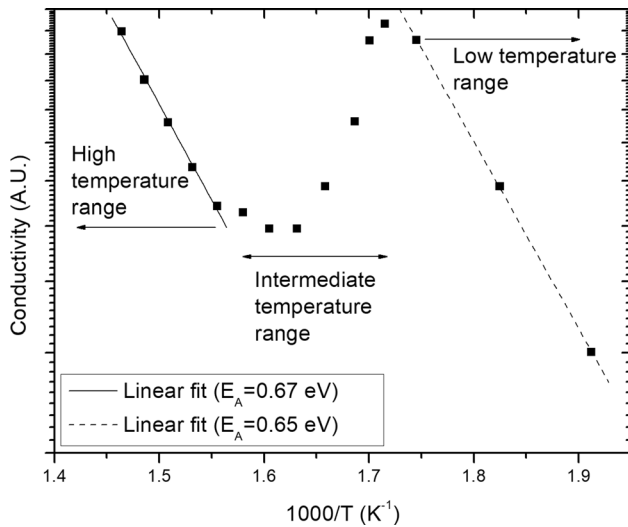
From the morphology of the ZnO nanorods, showing a large surface-to-volume ratio, in the range of  $10^4 \text{ cm}^{-1}$ , different surface phenomena might be expected as it has already been reported in this type of oxide by Major et al. [56] who studied the electrical properties in ZnO films deposited by spray pyrolysis and highlighted the transport properties as a function of different environments and temperatures, considering in detail the surface phenomena in them. Mandal et al. [52] studied also the transport properties of ZnO nanorods, but without considering the surface phenomena. In this last section, we addressed the effect of surface phenomena in the transport properties of the ZnO nanorods carrying out impedance spectroscopy measurements as a function of temperature.

Figure 8 shows the impedance spectra in the complex plane (real versus imaginary impedance) for film F1. When the sample was measured at low

temperatures, the film showed a very high impedance, indicating a very resistive film. Reliable measurements were obtained once the temperature was above 473 K, just when the impedance spectra showed a clear and almost ideal arc. By means of an equivalent circuit, and using the Z-VIEW Program, the arc was fitted appropriately by a single RC circuit in parallel, see inset in Fig. 8. From the fitting results, the capacitance  $C$  was found in the range of  $\sim (7.8\text{--}8.6) \times 10^{-12} \text{ F}$ , which corresponded to the bulk or grain of the ZnO film [57]. The latter value of the capacitance is similar to the one shown by ZnO films deposited by other techniques [58]. The resistance  $R$  (or more properly, its inverse  $\frac{1}{R}$ , related to the conductance) of the fitted circuit for each temperature was also computed and it was plotted as a function of  $\frac{1}{T}$  in Fig. 9. In this figure, it can be appreciated three different zones: at low temperatures ( $\sim 550$  to  $580 \text{ K}$ ), it is observed an increase in the conductivity with the increment of temperature (region 1). At the intermediate temperature range ( $\sim 590$  to  $620 \text{ K}$ ), it is highlighted a decrease in the conductivity with the increment of temperature (region 2). Finally, for temperatures over  $630 \text{ K}$  and up to  $\sim 680 \text{ K}$ , a new increase in the electrical conductivity was observed. For regions 1 and 3, the conductivity was considered to follow an Arrhenius type behavior  $\sim \exp\left(-\frac{E_A}{k_B T}\right)$ , where  $E_A$ ,  $k_B$  and  $T$  are the activation energy, the Boltzmann constant and the absolute temperature, respectively. Upon a linear fitting, the estimation of



**Fig. 8** Impedance complex spectra for a ZnO nanorod thin film (film F1), measured at 623 and 653 K. The inset shows the equivalent RC circuit that best fitted the experimental data



**Fig. 9** Estimation of the activation energy for conductivity for a ZnO nanorod thin film (film F1). The electronic transport showed three regions of conductivity as the temperature during measurement increased

the activation energy for region 3 and 1 were of:  $0.67 \pm 0.02$  eV and  $0.65 \pm 0.01$  eV, corresponding to the high and low-temperature regions, respectively. Both activation energies were very close, indicating probably a unique electronic phenomenon in the semiconductor (which will be explained below). In the same way, Fig. 10 shows the  $\frac{1}{R}$  vs  $\frac{1}{T}$  plot for film F2, showing a similar phenomenon related to the conductivity as a function of the temperature. The activation energy in the high-temperature region was

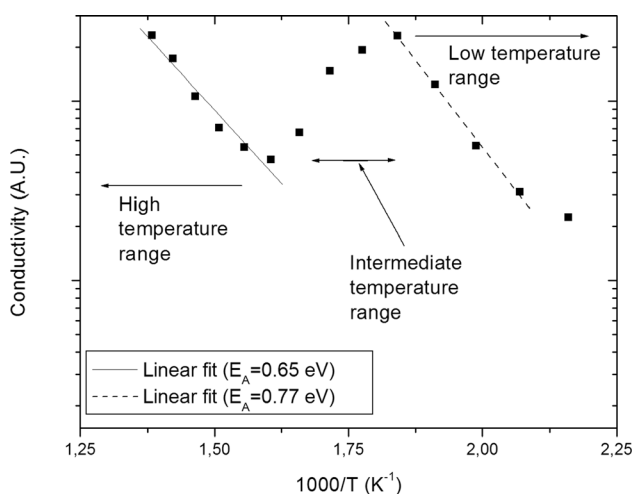


**Fig. 10** Estimation of the activation energy for conductivity for a ZnO nanorod thin film (film F2). The electronic transport showed three regions of conductivity as the temperature during measurement increased

about  $0.65 \pm 0.06$  eV and  $0.77 \pm 0.04$  eV in the low-temperature range. The average capacitance was found in the range of  $10^{-11}$  F, which might be related to bulk properties of the oxide. Major et al. [56], studied the annealing behavior of the electrical properties in vacuum, air and oxygen of ZnO films deposited by spray pyrolysis. According to his work, the behavior of the resistivity with annealing temperature can be explained from chemisorption and desorption of oxygen at the grain boundaries. The chemisorption of oxygen on the ZnO surfaces gives rise to surface acceptor states. The observed behavior of the resistivity with annealing temperature can be attributed to the creation and annihilation of oxygen acceptor states at the grain boundaries which act as traps for electrons. The grain boundary carrier-trapping model can explain the annealing behavior. The model states that if the density of trap states is high and is comparable with the carrier concentration in the grains, a severe depletion of carriers will occur throughout the bulk of the grains; however, the excitation of carriers from the trap states to the conduction band results in a temperature dependence of the carrier concentration  $n = n_o \exp\left(-\frac{E_c - E_t}{k_B T}\right)$ , where  $E_c$  and  $E_t$  are the positions of the conduction band edge and the trap level, respectively [56].

In our work, ZnO nanorod films F1 showed an intermediate temperature region  $\sim 580$ – $630$  K in which the conductivity decreased. For film F2 this temperature range was observed at  $\sim 543$ – $620$  K. However, for temperatures below (low-temperature range) and above (high-temperature range) the noticed regions, the conductivity increased, Figs. 9 and 10. Considering the model proposed by Major et al. [56] it is possible to explain the above result. During the synthesis by CBD and the annealing of the ZnO nanorod films, oxygen could be chemisorbed at the grain boundaries, giving rise to a high density of trap states, leading to a dramatic depletion of carriers in the grains. This results in a large increase in the resistivity that is achieved by the sample in the low and high-temperature ranges. In these stages the large depletion of carriers is so great that further chemisorption or desorption has little effect and the temperature dependence on the conductivity is governed by the excitation of electrons from trap levels to the conduction band, showing activation energies of 0.65 eV and 0.67 eV in the low and high-temperature ranges, respectively, for ZnO nanorod film F1 (Fig. 9),

and 0.77 eV and 0.65 eV in the low and high-temperature ranges, respectively, for film F2 (Fig. 10). These activation energies are attributed to the appearance of trap states due to the chemisorption of oxygen at the ZnO grain boundaries. Similar activation energies are found in film F1; however, film F2 show a small deviation of the activation energy in the low-temperature range which could be attributed to other trapping states or to the spread of energy of the trap states [56]. Major et al. estimated an activation energy of 0.51 eV in his ZnO films deposited by spray pyrolysis [56]. In contrast, in the intermediate temperature ranges for both films it was observed a noticeable increase in the resistivity (decrease in the conductivity). It is possible that these regions are probably dramatically governed by chemisorption or desorption phenomena at the ZnO surfaces.

## 4 Conclusions

High-quality ZnO nanorods films were synthesized by CBD techniques at low temperatures on glass substrates using two different ratios of HMTA:ZnAc. The structural, optical and electronic properties were studied in the films. The ZnO nanorod films resulted polycrystalline, showing the hexagonal wurtzite structure and were grown partially oriented along the (002) direction. The ZnO nanorod films showed a crystallite size about 50–55 nm with a dislocation density in the range of  $10^{15}$  lines- $m^{-2}$ , a strain in the range of  $10^{-3}$  and a high surface-to-volume ratio  $\sim 10^4$   $cm^{-1}$ . ZnO nanorods films synthesized with the lowest ratio of HMTA:ZnAc resulted thinner and shorter with a fair orientation compared to films synthesized with the highest ratio. Energy dispersive spectroscopy and photoluminescence measurements indicated the existence of oxygen vacancies in the films. The ZnO nanorod films showed a bandgap energy about 3.24 eV. From photoluminescence results, a more intense ultraviolet excitonic emission band was observed in the films synthesized with the lowest ratio of HMTA:ZnAc compared with the wide defect band attributed to point defects. The non-stoichiometry of the films resulted in a carrier concentration in the range of  $10^{15}$  and  $10^{16}$   $cm^{-3}$ , for the ZnO nanorods films synthesized with the low and high ratio of HMTA:ZnAc, respectively. Finally, from impedance spectroscopy measurements, a noticeable temperature-dependent electronic conductivity was

observed in the films, related probably to the nanostructured morphology. In both films it was observed that the electronic conductivity decreased in the intermediate temperature region with the increment of temperature, probably due to chemisorption or desorption phenomena. But the electronic conductivity in the low and the high-temperature regions obeyed the grain boundary carrier-trapping model with the increment of the temperature showing in both regions an activation energy close to 0.6 eV, attributed to the appearance of trap states due to the chemisorption of oxygen at the grain boundaries of the ZnO nanorods. Table 1 resumes the electronic properties of the ZnO nanorods.

## Acknowledgements

The authors would like to acknowledge the financial support from Secretaría de Investigación y Posgrado del Instituto Politécnico Nacional, México. We also wish to thank to Consejo Nacional de Ciencia y Tecnología, México, under Grant Number CB-2015/253342.

## Funding

The authors would like to acknowledge the financial support from Secretaría de Investigación y Posgrado del Instituto Politécnico Nacional, México, and to Consejo Nacional de Ciencia y Tecnología, México, Grant Number CB-2015/253342.

## Declarations

**Conflict of interest** There are no conflicts of interest.

## References

1. Ü. Özgür, D. Hofstetter, H. Morkoç, Proc. IEEE (2010). <https://doi.org/10.1109/JPROC.2010.2044550>
2. M. Scharrer, A. Yamilov, X. Wu, H. Cao, R.P.H. Chang, Appl. Phys. Lett. (2006). <https://doi.org/10.1063/1.2203939>
3. Ü. Özgür, Y.I. Alivov, C. Liu, A. Teke, M.A. Reshchikov, S. Doğan, V. Avrutin, S.J. Cho, H. Morkoç, J. Appl. Phys. (2005). <https://doi.org/10.1063/1.1992666>
4. I. Gonzalez-Valls, M. Lira-Cantu, Energy Environ. Sci. (2009). <https://doi.org/10.1039/B811536B>

5. M. Dinescu, P. Verardi, *Appl. Surf. Sci.* (1996). [https://doi.org/10.1016/S0169-4332\(97\)80013-X](https://doi.org/10.1016/S0169-4332(97)80013-X)
6. P. Verardi, M. Dinescu, A. Andrei, *Appl. Surf. Sci.* (1996). [https://doi.org/10.1016/0169-4332\(95\)00591-9](https://doi.org/10.1016/0169-4332(95)00591-9)
7. K.L. Narasimhan, S.P. Pai, V.R. Palkar, R. Pinto, *Thin Solid Films* (1997). [https://doi.org/10.1016/S0040-6090\(96\)09157-2](https://doi.org/10.1016/S0040-6090(96)09157-2)
8. H.S. Yoon, K.S. Lee, T.S. Lee, B. Cheong, D.K. Choi, D.H. Kim, W.M. Kim, *Sol. Energy Mater. Sol. Cells* (2008). <https://doi.org/10.1016/j.solmat.2008.05.010>
9. H. Enoki, T. Nakayama, J. Echigoya, *Phys. Status Solidi* (1992). <https://doi.org/10.1002/pssa.2211290116>
10. R. Wendt, K. Ellmer, *Surf. Coat. Technol.* (1997). [https://doi.org/10.1016/S0257-8972\(97\)00036-4](https://doi.org/10.1016/S0257-8972(97)00036-4)
11. A.F. Abdulrahman, S.M. Ahmed, N.M. Ahmed, *Sci. J. UOZ* 5(1), 128 (2017). <https://doi.org/10.25271/2017.5.1.313>
12. B.P. Zhang, N.T. Binh, K. Wakatsuki, Y. Segawa, Y. Yamada, N. Usami, M. Kawasaki, H. Koinuma, *Appl. Phys. Lett.* (2004). <https://doi.org/10.1063/1.1753061>
13. T.M. Barnes, J. Leaf, C. Fry, C.A. Wolden, *J. Cryst. Growth* (2005). <https://doi.org/10.1016/j.jcrysgro.2004.10.015>
14. J. Hu, R.G. Gordon, *J. Appl. Phys.* (1992). <https://doi.org/10.1063/1.351309>
15. K. Govender, D.S. Boyle, P.B. Kenway, P. O'Brien, *J. Mater. Chem.* (2004). <https://doi.org/10.1039/B404784B>
16. G. Hodes, *Chemical Solution Deposition of Semiconductor Films* (CRC Press, Boca Raton, 2002), pp. 266–271
17. A.F. Abdulrahman, S.M. Ahmed, N.M. Ahmed, M.A. Almessiere, *Crystals* 10, 386 (2020). <https://doi.org/10.3390/cryst10050386>
18. L.L. Yang, Q.X. Zhao, M. Willander, *J. Alloys Compd.* (2009). <https://doi.org/10.1016/j.jallcom.2008.08.002>
19. R. Pietruszka, B.S. Witkowski, S. Gieraltowska, P. Caban, L. Wachnicki, E. Zielony, K. Gwozdz, P. Bieganski, E. Placzek-Popko, M. Godlewski, *Energy Mater. Sol. Cells.* (2015). <https://doi.org/10.1016/j.solmat.2015.06.042>
20. G.C. Yi, C. Wang, W. Il Park, *Semicond. Sci. Technol.* (2005). <https://doi.org/10.1088/0268-1242/20/4/003>
21. S.W. Kim, T. Kotani, M. Ueda, S. Fujita, S. Fujita, *Appl. Phys. Lett.* (2003). <https://doi.org/10.1063/1.1622795>
22. W.L. Xu, M.J. Zheng, G.Q. Ding, W.Z. Shen, *Chem. Phys. Lett.* (2005). <https://doi.org/10.1016/j.cplett.2005.05.105>
23. X.D. Bai, P.X. Gao, Z.L. Wang, E.G. Wang, *Appl. Phys. Lett.* (2003). <https://doi.org/10.1063/1.1587878>
24. C. Ronning, P.X. Gao, Y. Ding, Z.L. Wang, D. Schwen, *Appl. Phys. Lett.* (2004). <https://doi.org/10.1063/1.1645319>
25. Y.B. Li, Y. Bando, T. Sato, K. Kurashima, *Appl. Phys. Lett.* (2002). <https://doi.org/10.1063/1.1492008>
26. J. Angulo-Rocha, O. Velarde-Escobar, C. Yee-Rendón, G. Atondo-Rubio, R. Millan-Almaraz, E. Camarillo-García, M. García-Hipólito, F. Ramos-Brito, *J. Lumin.* (2017). <https://doi.org/10.1016/j.jlumin.2017.01.026>
27. G.N. Panin, H.D. Cho, S.W. Lee, T.W. Kang, *J. Korean Phys. Soc.* (2014). <https://doi.org/10.3938/jkps.64.1403>
28. S.J. An, G.C. Yi, *Appl. Phys. Lett.* (2007). <https://doi.org/10.1063/1.2786852>
29. S.W. Lee, H.D. Cho, G. Panin, T. Won Kang, *Appl. Phys. Lett.* (2011). <https://doi.org/10.1063/1.3562608>
30. A.F. Abdulrahman, S.M. Ahmed, N.M. Ahmed, M.A. Almessiere, *AIP Conf. Proc.* 1875, 020004 (2017). <https://doi.org/10.1063/1.4998358>
31. A. Fattah, S.M. Ahmed, N.M. Ahmed, *Sci. J. Univ. Zakho* 6(4), 160 (2018). <https://doi.org/10.25271/sjuoz.2018.6.4.546j>
32. L. Znaidi, *Mater. Sci. Eng. B* (2010). <https://doi.org/10.1016/j.mseb.2010.07.001>
33. J. Song, S. Lim, *J. Phys. Chem. C* (2007). <https://doi.org/10.1021/jp0655017>
34. N.T. Son, J.-S. Noh, S. Park, *Appl. Surf. Sci.* (2016). <https://doi.org/10.1016/j.apsusc.2016.04.107j>
35. S. Guillemin, E. Appert, H. Roussel, B. Doisneau, R. Parize, T. Boudou, G. Bremond, V. Consonni, *J. Phys. Chem. C* (2015). <https://doi.org/10.1021/acs.jpcc.5b06180>
36. Y. Tao, M. Fu, A. Zhao, D. He, Y. Wang, *J. Alloys Compd.* (2010). <https://doi.org/10.1016/j.jallcom.2009.09.020>
37. J.B. Cui, C.P. Daghljan, U.J. Gibson, R. Püsche, P. Geithner, L. Ley, *J. Appl. Phys.* (2005). <https://doi.org/10.1063/1.1854206>
38. C. He, Z. Zheng, H. Tang, L. Zhao, F. Lu, *J. Phys. Chem. C* (2009). <https://doi.org/10.1021/jp902523c>
39. S.Y. Liu, T. Chen, J. Wan, G.P. Ru, B.Z. Li, X.P. Qu, *Appl. Phys. A* (2009). <https://doi.org/10.1007/s00339-008-4957-5>
40. K.L. Foo, U. Hashim, K. Muhammad, C.H. Voon, *Nanoscale Res. Lett.* (2014). <https://doi.org/10.1186/1556-276X-9-429>
41. H. Zhang, X. Quan, S. Chen, H. Zhao, *Appl. Phys. A* (2007). <https://doi.org/10.1007/s00339-007-4167-6>
42. J.W.P. Hsu, Z.R. Tian, N.C. Simmons, C.M. Matzke, J.A. Voigt, J. Liu, *Nano Lett.* (2005). <https://doi.org/10.1021/nl048322e>
43. S. Fujihara, C. Sasaki, T. Kimura, *Appl. Surf. Sci.* (2001). [https://doi.org/10.1016/S0169-4332\(01\)00367-1](https://doi.org/10.1016/S0169-4332(01)00367-1)
44. M.N.R. Ashfold, R.P. Doherty, N.G. Ndifor-Angwafor, D.J. Riley, Y. Sun, *Thin Solid Films* (2007). <https://doi.org/10.1016/j.tsf.2007.03.122>
45. S.R. Morrison, *Adv. Catal.* (1955). [https://doi.org/10.1016/S0360-0564\(08\)60529-5](https://doi.org/10.1016/S0360-0564(08)60529-5)
46. R.J.D. Tilley, *Defects in Solids* (Wiley, Hoboken, NJ, 2008), pp. 147–148
47. A.F. Abdulrahman, *J. Mater. Sci.: Mater. Electron.* (2020). <https://doi.org/10.1007/s10854-020-03995-3>

48. H. Félix-Quintero, J. Angulo-Rocha, S.H. Murrieta, A.J. Hernández, G.E. Camarillo, J.M.C. Flores, C. Alejo-Armenta, M. García-Hipolito, F. Ramos-Brito, J. Lumin. (2017). <https://doi.org/10.1016/j.jlumin.2016.09.049>
49. P. Raghu, N. Srinatha, C.S. Naveen, H.M. Mahesh, B. Angadi, J. Alloys Compd. **694**, 68–75 (2016). <https://doi.org/10.1016/j.jallcom.2016.09.290>
50. G. Kortüm, *Reflectance Spectroscopy* (Springer, Heidelberg, 1969), pp. 170–216
51. F. Ramos-Brito, C. Alejo-Armenta, M. García-Hipólito, E. Camarillo, A.J. Hernández, C. Falcony, H.S. Murrieta, J. Lumin. (2011). <https://doi.org/10.1016/j.jlumin.2010.12.017>
52. S. Mandal, K. Sambasivarao, A. Dhar, S.K. Ray, J. Appl. Phys. (2009). <https://doi.org/10.1063/1.3168489>
53. N. Gogurla, S. Bayan, P. Chakrabarty, S.K. Ray, J. Lumin. (2018). <https://doi.org/10.1016/j.jlumin.2017.09.044>
54. P. Chakrabarty, M. Banik, N. Gogurla, S. Santra, S.K. Ray, R. Mukherjee, ACS Omega (2019). <https://doi.org/10.1021/acs.omega.9b01116>
55. R.A. Swalin, *Thermodynamics of Solids*, 2nd edn. (Wiley, Hoboken, 1972), pp. 335–341
56. S. Major, A. Banerjee, K.L. Chopra, Thin Solid Films (1984). [https://doi.org/10.1016/0040-6090\(84\)90376-6](https://doi.org/10.1016/0040-6090(84)90376-6)
57. J.T.S. Irvine, D.C. Sinclair, A.R. West, Adv. Mater. (1990). <https://doi.org/10.1002/adma.19900020304>
58. S. Kim, J. Maier, Electrochem. Solid-State Lett. (2003). <https://doi.org/10.1149/1.1613071>

**Publisher's Note** Springer Nature remains neutral with regard to jurisdictional claims in published maps and institutional affiliations.